MNRAS 000, 1–9 (2016) Preprint 11 May 2016 Compiled using MNRAS LATEX style file v3.0

Evidence for a direct collapse black hole in the Lyman α source CR7

Aaron Smith,[1]⋆ Volker Bromm[1] and Abraham Loeb[2]
[1]Department of Astronomy, The University of Texas at Austin, Austin, TX 78712, USA
[2]Department of Astronomy, Harvard University, 60 Garden Street, Cambridge, MA 02138, USA

Accepted 2016 May 10. Received 2016 May 10; in original form 2016 February 24

arXiv:1602.07639v2 [astro-ph.GA] 10 May 2016

ABSTRACT

Throughout the epoch of reionization the most luminous Lyα emitters are capable of ionizing their own local bubbles. The CR7 galaxy at $z \approx 6.6$ stands out for its combination of exceptionally bright Lyα and He II 1640 Å line emission but absence of metal lines. As a result CR7 may be the first viable candidate host of a young primordial starburst or direct collapse black hole. High-resolution spectroscopy reveals a +160 km s^{-1} velocity offset between the Lyα and He II line peaks while the spatial extent of the Lyα emitting region is $\sim$ 16 kpc. The observables are indicative of an outflow signature produced by a strong central source. We present one-dimensional radiation-hydrodynamics simulations incorporating accurate Lyα feedback and ionizing radiation to investigate the nature of the CR7 source. We find that a Population III star cluster with 10^5 K blackbody emission ionizes its environment too efficiently to generate a significant velocity offset. However, a massive black hole with a nonthermal Compton-thick spectrum is able to reproduce the Lyα signatures as a result of higher photon trapping and longer potential lifetime. For both sources, Lyα radiation pressure turns out to be dynamically important.

Key words: galaxies: formation – galaxies: high-redshift – cosmology: theory.

1 INTRODUCTION

Before the formation of the first stars and galaxies the cold, expanding Universe was in a state known as the cosmic dark ages. Eventually, gravitational instabilities seeded the growth of dark matter minihaloes with typical mass $M_{\rm h} \sim 10^{5-7}$ M$_\odot$, hosting a generation of massive Population III (Pop III) stars with a primordial gas composition. The first stars began the process of reionizing the Universe. Over time several of these haloes merge to form atomic cooling haloes with typical mass $M_{\rm h} \sim 10^{7-9}$M$_\odot$ by $z \sim 10$, corresponding to the first *bona fide* galaxies (Bromm & Yoshida 2011; Loeb & Furlanetto 2013). By this time star formation likely consisted of both Pop III and metal enriched Pop II stars (Jeon et al. 2015), although in principle pockets of pristine gas could persist to later redshifts (Pallottini et al. 2014; Ma et al. 2015). In addition to chemical evolution, the first galaxies experienced significant radiative and mechanical feedback (Pawlik et al. 2013). Understanding the formation of the first galaxies and their subsequent evolution provides important insights on the remainder of cosmic history and the transition to present-day galaxies.

The high-z observational frontier is constrained by the ability of current infrared technologies to detect increasingly faint and distant galaxies. However, the upgraded capabilities of the *Hubble Space Telescope* (*HST*) in combination with large aperture ground-based observatories has allowed deep broadband photometry and spectroscopic confirmation of a number of galaxies at $z > 6.5$ (Bouwens et al. 2011; Finkelstein et al. 2013; Oesch et al. 2015; Stark et al. 2015; Zitrin et al. 2015). As predicted by Partridge & Peebles (1967), proto-galactic star formation would produce powerful intrinsic Lyα luminosities, although the increasing neutral hydrogen fraction in the diffuse intergalactic medium (IGM) significantly suppresses Lyα transmission for sources at $z > 6.5$ (Dijkstra 2014; Mesinger et al. 2015). Still, galaxies with strong Lyα emission are more likely to be detected with substantial outflows or clustered within locally ionized bubbles and web-like morphologies (Jensen et al. 2013; Kakiichi et al. 2015; Smith et al. 2015). Despite attenuation from the neutral IGM one might hope to infer properties of the emission source, galaxy, and IGM based on the altered Lyα line profile, physical size of the Lyα emitting region, continuum spectral energy distribution (SED), and relative strength of Lyα, Hα, and He II 1640 Å nebular emission lines (Schaerer 2002; Johnson et al. 2009; Pawlik et al. 2011).

Recent follow-up observations of the Lyα emitter "CR7" (COSMOS redshift 7) at $z = 6.6$ by Sobral et al. (2015) confirmed the presence of strong He II emission with no detection of metal lines from the UV to the near infrared (see also Matthee et al. 2015). As the most luminous Lyα emitter at $z > 6$, the CR7 source may be the first detection of a massive ($\gtrsim 10^7$ M$_\odot$) Pop III star cluster. Deep *HST* imaging reveals three clumps (A, B, and C) in close proximity ($\sim$ 5 kpc). Component A dominates the rest-frame UV and is also coincident with both the He II emission and the centre of the Lyα emitting region. Clumps B and C are much redder and likely dominate the mass of the system. Because a normal stellar population fails to reproduce the excess Lyα and He II luminosities,

⋆ E-mail: asmith@astro.as.utexas.edu

© 2016 The Authors

Sobral et al. (2015) suggest a composite spectrum in which clump A is fit by a pure Pop III SED and clumps B+C are comprised of enriched populations. If CR7 does indeed host a Pop III star cluster with a top-heavy initial mass function (IMF) then we are likely viewing a rare starburst with an age of less than a few Myr (Pallottini et al. 2015; Hartwig et al. 2015; Visbal et al. 2016).

On the other hand, the Lyα emission from CR7 may also be due to accretion onto a ($\sim 10^{5-6}$ M$_\odot$) black hole. At this redshift the black hole growth time would have been limited to perhaps $\lesssim 500$ Myr providing a strong case for so-called "direct collapse" black holes (DCBHs) (Bromm & Loeb 2003), especially given the existence of supermassive black holes (SMBHs) of a few billion solar masses observed in $z > 6$ quasars (Fan et al. 2006). The DCBH formation scenario is explored in detail for the CR7 Lyα emitter with the models of Pallottini et al. (2015), Agarwal et al. (2015), and Smidt et al. (2016). Furthermore, Hartwig et al. (2015) use merger tree models to statistically argue against a Pop III starburst explanation based on their short lifetimes and earlier metal enrichment. Either way, the CR7 enigma is that a massive system was able to maintain a low-metallicity environment down to $z = 6.6$. However, under optimistic assumptions a DCBH is a likely outcome for pristine haloes exposed to strong Lyman-Werner radiation (Hartwig et al. 2015). Despite the theoretical uncertainties regarding its nature, the CR7 source has tantalizing significance as it opens up additional possibilities for direct observational constraints on first galaxy and quasar formation.

The remainder of this paper is devoted to a discussion of Lyα radiative transfer and radiation pressure in the context of the CR7 source. Stellar feedback has been observed to drive molecular gas outflows in the SDSS J0905+57 (redshift $z = 0.712$) compact starburst galaxy (Geach et al. 2014), and we expect a similar mechanism to operate for Lyα radiation pressure in high-z, low metallicity environments (Dijkstra & Loeb 2008, 2009). For a discussion of Lyα feedback in a more general context see Smith et al. (2016). In the case of the CR7 Lyα emitter, high-resolution spectroscopy has revealed a $+160$ km s^{-1} velocity offset between the Lyα and He II line peaks, which is indicative of an outflow signature and/or Lyα scattering in the IGM (Sobral et al. 2015). A redshifted Lyα line is common in Lyman-α emitting galaxies at $z \lesssim 3$ (Steidel et al. 2010; Erb et al. 2014; Hashimoto et al. 2015; Yang et al. 2016), nonetheless it is particularly interesting to consider Lyα radiation pressure assisted outflows in the context of CR7. An additional constraint from CR7 (clump A) is the spatial extent of the Lyα emitting region ($\sim$ 16 kpc physical). We therefore examine the effect of radiative feedback on these Lyα observables, including Lyα photon trapping and ionizing radiation. In Section 2 we introduce our simulation model and methodology. In Section 3 we present the radiation hydrodynamics and Lyα radiative transfer results. Finally, in Section 4 we provide a summary and conlusions.

2 MODELING THE CR7 SYSTEM

2.1 Basic observational properties

The luminous Lyα emitter CR7 at $z \approx 6.604^{+0.001}_{-0.003}$ stands out for its exceptional Lyα and He II 1640 Å line emission but absence of metal lines. High-resolution spectroscopy reveals a narrow Lyα line with a FWHM width of 266 ± 15 km s^{-1} and luminosity of $L_\alpha > 8.32 \times 10^{43}$ erg s^{-1}. This is a lower limit because a significant fraction of the Lyα photons could have been 'eliminated' from the line of sight due to radiative transfer effects within the galaxy, absorption by dust, anisotropic escape, and scattering by residual H I in the IGM. The He II 1640 Å line emission on the other hand is free from these complications, therefore we assume the observed luminosity of $L_{\rm He\,II} = 1.95{\times}10^{43}$ erg s^{-1} accounts for the entire emission. This implies a line ratio of He II/Ly$\alpha \lesssim 0.22$ and an ionizing flux ratio of $Q({\rm He^+})/Q({\rm H}) \lesssim 0.42$, corresponding to a hard blackbody spectrum with effective temperature $T_{\rm eff} > 100$ kK (Bromm et al. 2001; Schaerer 2002).

The observed CR7 properties provide a strong case for either a young primordial starburst or direct collapse black hole. Given that the halo mass of clump A is $M_{\rm h,A} \approx 3 \times 10^{10}$ M$_\odot$ and the baryonic mass is $M_{\rm gas,A} \lesssim 5 \times 10^9$ M$_\odot$ it is not impossible for a massive ($\gtrsim 10^7$ M$_\odot$) Pop III star cluster to produce the observed He II emission, although this is pushing standard star formation theory to the extreme. In comparison, Pop II stars fall short by many orders of magnitude (Hartwig et al. 2015). Furthermore, the nondetection of metal lines strongly suggests that supernova feedback is not present in CR7. The relatively narrow Lyα line eliminates the possibility of Wolf-Rayet stars and active galactic nuclei (AGN) as the Lyα source as they produce broader lines with FWHM $\gtrsim 10^3$ km s^{-1} (Brinchmann et al. 2008). The proposal that CR7 is powered by a DCBH does not necessarily imply a similarly broad Lyα line. Quasar lines originate from the broad line region (BLR) near the vicinity of the black hole, which is made of small gas clouds each contributing a narrow portion of the broad line according to its line-of-sight velocity. The narrow line could be due to recombinations and resonant scattering not associated with a fully developed BLR, or to narrowing during transmission through the IGM.

The $+160$ km s^{-1} velocity offset between the Lyα and He II line peaks is most likely caused by an outflow within clump A. It is important to consider the uncertainty on the velocity offset, which is associated with the measured Lyα line width, the redshift estimates, and the spectral resolution. Although the line is broader than the offset it is sharply peaked so the FWHM greatly overestimates the uncertainty. The redshift confidence range $\sigma_z \approx 0.001$ implies a potential redshift uncertainty of at least $\sigma_{\Delta v,z} \approx c\sigma_z/(1+z) \approx 40$ km s^{-1}. The spectral resolution of DEIMOS/Keck was 0.65 Å pix^{-1}, which corresponds to an uncertainty of $\sigma_{\Delta v,{\rm Keck}} \approx c\Delta\lambda/[\lambda_\alpha(1+z)] \approx 21.1$ km s^{-1}. The NIR observations with X-SHOOTER/VLT had a resolution of $R \sim 5300$, corresponding to $\sigma_{\Delta v,{\rm VLT}} \approx c/R \approx 56.6$ km s^{-1} (Sobral et al. 2015). The spatial extent of the Lyα emitting region is concentrated well within the virial radius of $r_{\rm vir,A} \approx 13.3$ kpc. If the offset was caused by scattering in the IGM the Lyα halo would be much more extended (Loeb & Rybicki 1999). Resonant scattering in a uniform static sphere requires an optical depth at line centre of $\tau_0 \approx 5{\times}10^6\, T_4^{-1}[\Delta v/(160\,{\rm km\,s^{-1}})]^3$ to produce the necessary offset, where we have normalized the gas temperature according to $T_4 \equiv T/(10^4$ K), see the discussion following equation (34) in Smith et al. (2015). Assuming an approximately isothermal density profile, clump A would have $\tau_0 \gtrsim 10^{11}$ if it remained neutral. Therefore, the effective optical depth must be reduced by a significant velocity gradient and ionization fraction. In this low-metallicity environment the possible outflow mechanisms are hydrodynamical gas pressure, ionizing radiation pressure, and Lyα radiation pressure. We therefore simulate each of these self-consistently in order to determine the effect on the key observables.

2.2 Numerical methodology

The simulations in this paper employ the Lyα radiation hydrodynamics (RHD) methods described and tested in Smith et al. (2016), which we briefly review now. For computational efficiency

and model simplicity we focus on spherically symmetric profiles for this paper. Therefore, we solve the RHD equations in the Lagrangian framework with derivatives denoted by the uppercase differential operator $D(\bullet)/Dt \equiv \partial(\bullet)/\partial t + \boldsymbol{v}\cdot\boldsymbol{\nabla}(\bullet)$. The equations for conservation of mass, momentum, and total energy with terms accurate to second order in (v/c) are

$$\frac{D\rho}{Dt} + \rho\boldsymbol{\nabla}\cdot\boldsymbol{v} = 0\,, \tag{1}$$

$$\frac{D\boldsymbol{v}}{Dt} + \frac{\boldsymbol{\nabla}P}{\rho} = -\boldsymbol{\nabla}\Phi + \boldsymbol{a}_\alpha + \boldsymbol{a}_\gamma\,, \tag{2}$$

$$\frac{D\epsilon}{Dt} + P\frac{D(1/\rho)}{Dt} = \frac{\Gamma-\Lambda}{\rho}\,, \tag{3}$$

where ρ is the density, $\boldsymbol{v}$ the velocity, P the pressure, and ϵ is specific internal energy. Our spherically symmetric hydrodynamics solver is based on the von Neumann-Richtmyer staggered mesh scheme described in von Neumann & Richtmyer (1950), Mezzacappa & Bruenn (1993), and Castor (2004). This has the advantage of adaptive resolution, allowing the grid to follow the motion of the gas. Artificial viscosity is included in order to damp numerical oscillations near shocks. Finally, we assume an ideal gas equation of state so the pressure is specified by $P = (\gamma_{\rm ad}-1)\rho\epsilon$, where in primordial gas we use an adiabatic index of $\gamma_{\rm ad} = 5/3$.

The source terms are related to the gravitational potential Φ, acceleration due to Lyα photons $\boldsymbol{a}_\alpha$, acceleration from ionizing radiation $\boldsymbol{a}_\gamma$, and volumetric photoionization heating minus radiative cooling rates, $\Gamma-\Lambda$. In our model the gravitational acceleration includes gas, dark matter, and dark energy components as $\boldsymbol{a}_{\rm grav} = -\boldsymbol{\nabla}\Phi = -GM_{<r}\hat{\boldsymbol{r}}/r^2 + H_0^2\Omega_\Lambda\boldsymbol{r}$, where $M_{<r}$ is the enclosed mass, H_0 is the Hubble constant, and Ω_Λ is the dark energy density in units of the present-day critical density. The dark energy component has a negligible effect at these redshifts but is included for completeness. Thus, we adopt physical units for cosmological simulations and directly account for Hubble flow via the initial velocity field. The Lyα radiation pressure is accurately calculated with the Cosmic Lyα Transfer code (COLT) according to the Monte-Carlo implementation described in Smith et al. (2015, 2016).

Because the ionization state of the gas can greatly affect Lyα radiative transfer we also self-consistently simulate ionizing radiation. We solve the time-dependent transfer equation in an explicitly photon-conserving manner in order to accurately follow the evolution of the ionization front (Abel et al. 1999). Following Pawlik & Schaye (2011) and Jeon et al. (2014) we collect the photons into three bands according to the ionization energies of H I, He I, and He II, or 13.6 eV, 24.6 eV, and 54.4 eV, respectively. Absorption and heating are treated in the grey approximation using the source intensity to compute the photon emission rates $\dot{N}_{{\rm ion},i}$ as well as expectation values for photoionization cross-sections $\langle\sigma_x\rangle_i$ and energy transfer per ionizing photon $\langle\varepsilon_x\rangle_i$, where the subscript $i \in \{1, 2, 3\}$ denotes the particular band and the subscript $x \in \{{\rm H\,I}, {\rm He\,I}, {\rm He\,II}\}$ denotes the species. These quantities completely describe the central source of ionizing radiation in our models. Finally, we also solve the rate equations for a primordial chemistry network consisting of H, H^+, He, He^+, He^{++}, and e^- (Bromm et al. 2002). Reactions affecting these abundances include photoionization, collisional ionization, and recombination while cooling mechanisms also include collisional excitation, bremsstrahlung, and inverse Compton cooling (Cen 1992). As photoionization can rapidly affect the chemical and thermal state of the gas we employ timestep sub-cycling to accurately follow the evolution.

For the initial simulation setup we adopt an idealized model galaxy with the observed properties of the CR7 system. For simplicity we assume an NFW dark matter halo profile and thereby calculate the dark matter gravitational contribution analytically. Specifically, the dark matter density is $\rho_{\rm DM}(r) = \rho_{\rm DM,0}R_{\rm S}^3/[r(R_{\rm S}+r)^2]$ with a concentration parameter of $c_{\rm NFW} \equiv R_{\rm vir}/R_{\rm S} \approx 5$, where $R_{\rm vir}$ is the virial radius and $R_{\rm S}$ is the scale radius. The gas follows an isothermal density profile with $\rho(r) = \rho_{\rm vir}(r/R_{\rm vir})^{-2}$ until it reaches the background IGM density $\rho_{\rm IGM}(z)$. The galactic gas starts off cold and neutral, with an initial temperature set by the cosmic microwave background at $T = 2.725\ {\rm K}\,(1+z)$. The exact value makes little difference as the gas quickly becomes hot and ionized within the growing H II region. The simulation begins at redshift $z = 6.6$ and continues for $10-100$ Myr.

2.3 Possible sources

The delayed Pop III starburst and massive black hole (MBH) scenarios are characterized by central emission with different source parameters. Each model is normalized to match the He II emission rate which we calculate to be $\dot{N}_{\rm He\,II} \approx 3.44\times10^{54}\ {\rm s}^{-1}$ (Bromm et al. 2001; Schaerer 2002). The specific source parameters for each model considered in this paper are presented in Table 1. The fiducial Pop III case is calculated from a blackbody spectrum with effective temperature $T_{\rm eff} = 100$ kK. We also consider modified scenarios in which (*i*) the Lyα luminosity is boosted by an order of magnitude and (*ii*) the ionizing emission rates are reduced by an order of magnitude as a crude approximation for continuum leakage within a one-dimensional setting. The $\sim 10^5\ {\rm M}_\odot$ black hole case is based on the popular DCBH formation model, although our use of the MBH acronym allows for other formation scenarios. We model the MBH according to the nonthermal Compton-thick spectrum presented by Pacucci et al. (2015). Specifically, we use the supplemental data provided by the authors to calculate typical ionization rates for their low-density profile, standard accretion scenario at $\lesssim 75$ Myr. The Pop III and MBH SEDs differ significantly, which is apparent by comparing the photon emission rates, photoionization cross-sections, and energy transfer per ionizing photon in Table 1. The Compton-thick MBH environment reprocesses the broadband spectrum such that only X-ray and non-ionizing photons remain. Note, for simplicity we model the cascade of multiple ionization and heating events experienced by the X-ray photons with a 'one-shot' approximation, where all the energy is transferred in a single scattering (e.g. Shull & van Steenberg 1985).

The ionizing photons are responsible for heating the gas within the galaxy and thereby produce a high-velocity shock. The Strömgren radius for such a strong source surrounded by the neutral IGM with a background density of $n_{\rm H\,I}|_{z=6.6} \approx 4.3\times10^{-4}\ {\rm cm}^{-3}$, Case B recombination coefficient $a_{\rm B} \approx 2.59\times10^{-13}{\rm cm}^3{\rm s}^{-1}$, and rate of ionizing photons $\dot{N}_{\rm ion} \approx 5\times10^{54}\ {\rm s}^{-1}$ is of order $r_{\rm S} \approx [3\dot{N}_{\rm ion}/(4\pi n_{\rm H\,I}^2\alpha_{\rm B})]^{1/3} \sim 1$ Mpc. Therefore, the CR7 source is capable of ionizing its own local super bubble. Furthermore, the ionization parameters and resultant state of the gas has a strong impact on the emergent Lyα spectra. The modifications to our fiducial models are designed to explore the impact of source parameters and gain additional physical insight.

3 SIMULATION RESULTS

3.1 Outflow Structure

Soon after the central source turns on the gas within the galaxy becomes hot and ionized. Eventually a dense shell forms in hy-

Table 1. Summary of the source parameters for the Pop III and black hole models. The 'boost' and 'leak' modifications respectively increase the Lyα luminosity or reduce the ionizing photon rate. The Lyα luminosity is taken to be $L_\alpha = 0.68 h\nu_\alpha (1 - f_{\rm esc}^{\rm ion}) \dot{N}_{\rm ion}$ where $h\nu_\alpha = 10.2$ eV, $f_{\rm esc}^{\rm ion}$ is the escape fraction of ionizing photons, and $\dot{N}_{\rm ion} = \sum \dot{N}_{{\rm ion},i}$.

Model	Pop III	Black Hole	Boost	Leak
L_α [erg s^{-1}]	6.53×10^{44}	3.82×10^{43}	$\times 10$	–
$\dot{N}_{\rm ion,1}$ [s^{-1}]	2.63×10^{55}	0	–	$\div 10$
$\dot{N}_{\rm ion,2}$ [s^{-1}]	2.90×10^{55}	0	–	$\div 10$
$\dot{N}_{\rm ion,3}$ [s^{-1}]	3.44×10^{54}	3.44×10^{54}	–	$\div 10$
$\dot{N}_{\rm ion}$ [s^{-1}]	5.88×10^{55}	3.44×10^{54}	–	$\div 10$
$\langle\sigma_{\rm H\,I}\rangle_1$ [cm^2]	3.00×10^{-18}	0	–	–
$\langle\sigma_{\rm H\,I}\rangle_2$ [cm^2]	5.69×10^{-19}	0	–	–
$\langle\sigma_{\rm H\,I}\rangle_3$ [cm^2]	7.88×10^{-20}	2.61×10^{-23}	–	–
$\langle\sigma_{\rm He\,I}\rangle_2$ [cm^2]	4.67×10^{-18}	0	–	–
$\langle\sigma_{\rm He\,I}\rangle_3$ [cm^2]	1.48×10^{-18}	7.42×10^{-21}	–	–
$\langle\sigma_{\rm He\,II}\rangle_3$ [cm^2]	1.05×10^{-18}	5.66×10^{-22}	–	–
$\langle\varepsilon_{\rm H\,I}\rangle_1$ [eV]	3.85	0	–	–
$\langle\varepsilon_{\rm H\,I}\rangle_2$ [eV]	17.5	0	–	–
$\langle\varepsilon_{\rm H\,I}\rangle_3$ [eV]	48.4	579	–	–
$\langle\varepsilon_{\rm He\,I}\rangle_2$ [eV]	8.01	0	–	–
$\langle\varepsilon_{\rm He\,I}\rangle_3$ [eV]	38.5	728	–	–
$\langle\varepsilon_{\rm He\,II}\rangle_3$ [eV]	7.89	550	–	–

drodynamical response and expands in accordance with conservation of momentum. If we assume the shell continually accumulates mass as it sweeps outward into an isothermal density profile then the mass grows with radius as $m(r) = 4\pi \int_0^r \rho(r') r'^2 dr' \propto r$. We may extend the analysis by considering power-law profiles with $m(r) = m_0 (r/r_0)^\beta$ where $\beta \in (0, 1)$ and the subscript 0 denotes a specified moment in time. Therefore, momentum conservation dictates that

$$\frac{{\rm d}(mv)}{{\rm d}t} = \frac{\rm d}{{\rm d}t}\left[m_0 \left(\frac{r}{r_0}\right)^\beta \dot{r} \right] = F(t)\,, \tag{4}$$

where $F(t)$ is the force on the shell. Examples of the force contributions are from Lyα photons $\sim L_\alpha/c$, gravity $\sim Gm(r)M(<r)/r^2 \propto r^{\beta-1}$, and gas pressure $\sim 4\pi r^2 \rho c_{\rm s}^2$ where $c_{\rm s}$ is the sound speed. In the case that these forces vary slowly in time or are small compared to the initial kick, Equation (4) admits the following power-law solution for the shell's motion:

$$f \equiv 1 + (1+\beta)\frac{(t-t_0)}{r_0}\left(v_0 + \frac{a_0}{2}(t-t_0)\right),$$
$$r(t) = r_0 f^{\frac{1}{1+\beta}} \qquad \text{and} \qquad v(t) = [v_0 + a_0(t-t_0)]\, f^{\frac{-\beta}{1+\beta}}\,, \tag{5}$$

where at time t_0 the radius, velocity, and acceleration are respectively r_0, v_0, and a_0. Equation (5) provides a reasonable description of the evolution at late times, despite the apparent breakdown in the validity of our assumptions early on. The radial expansion of the shells in each of the simulation models is shown in Fig. 1. The shell maintains a $v_{\rm sh} \gtrsim 100$ km s^{-1} outflow throughout the simulation. We also show that Lyα radiation pressure significantly impacts the shell velocity, which is evident in comparison to simulations without Lyα coupling included. Furthermore, as expected, the Lyα feedback is noticeably more effective in the models with a boost in Lyα luminosity or an ionizing continuum leakage.

Similarly, we present radial profiles of the gas number density and velocity at various stages throughout the MBH simulation in Fig. 2. The evolution of the shell outflow is qualitatively similar in each of the models with slight differences in shape. At late times, e.g. as reflected in the 60 Myr curve, the sharp shock features natu-

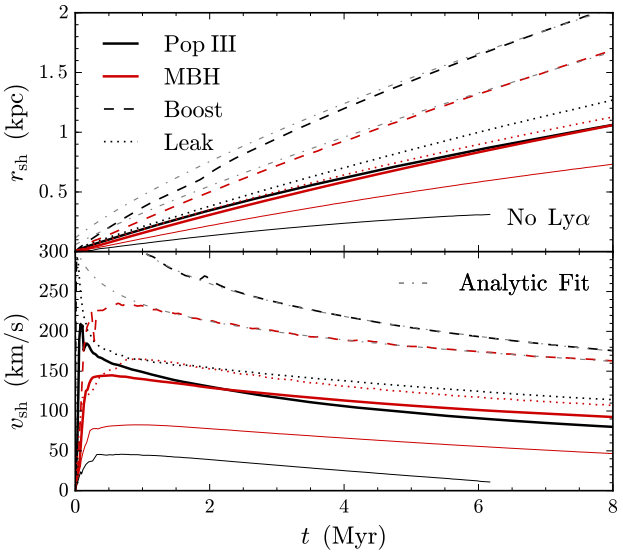


Figure 1. Radial position $r_{\rm sh}$ and velocity $v_{\rm sh}$ of the expanding shell for each model. The Pop III and MBH models are shown by the solid black and red curves, while the Boost and Leak modifications are denoted by dashed and dotted curves of the corresponding color. The grey dash-dotted curves are fits using Equation (5), only provided for the Boost models to avoid overcrowding the figure. For reference, $\beta = 0.26$ (0.15) for the Pop III (MBH) Boost case. The thin curves represent simulations without Lyα coupling, demonstrating that Lyα radiation pressure is dynamically important. The radius was selected based on the peak number density within the shell.

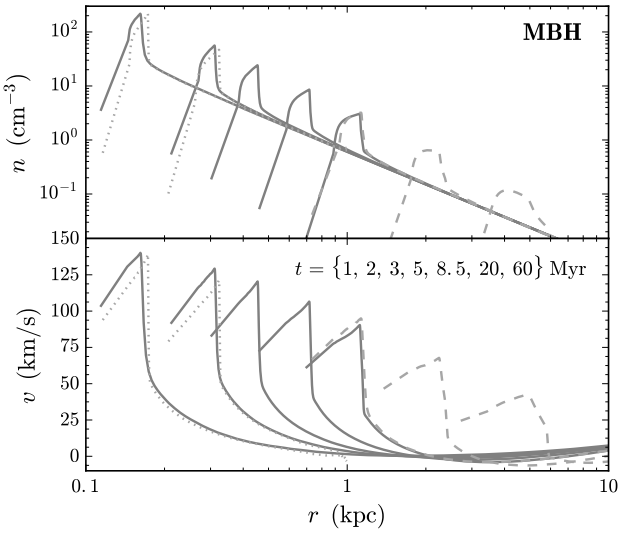


Figure 2. Evolution of the gas number density n and velocity v for $t = \{1, 2, 3, 5, 8.5, 20, 60\}$ Myr for the MBH model. The dotted curves are from a higher resolution simulation while the dashed curves are from a lower resolution simulation. The shell outflow structure is the predominant feature throughout the hydrodynamical simulation. The other models also exhibit qualitatively similar radial profiles.

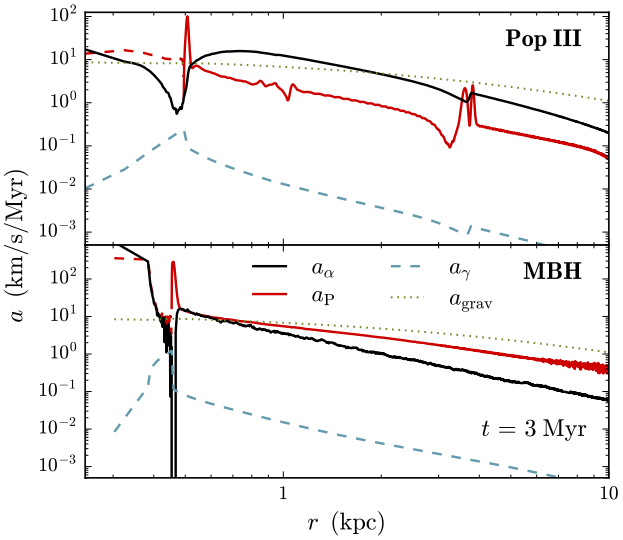


Figure 3. Radial profile of the acceleration due to Lyα photons a_α, gas pressure a_P, ionizing radiation a_γ, and gravity a_{grav} (dark matter + baryons). Both the Pop III (upper) and MBH (lower) models are shown 3 Myr into the simulation. Lyα trapping can be quite significant. We note that $a_P < 0$ inside the shell due to a negative pressure gradient (shown as dashed lines).

rally dissipate as it continues to propagate into lower density gas. In Fig. 3 we consider the radial acceleration due to Lyα photons, gas pressure, ionizing radiation, and gravity (dark matter + baryons). The relative importance of Lyα feedback and hydrodynamical pressure is inverted between the Pop III and MBH cases. In the massive black hole case Lyα radiation undergoes significant trapping within the shell and Lyα feedback is dominant within the shell. However, due to resonant scattering in expanding media the photons emerge redward of line centre and therefore the Lyα force is reduced. One of the predominant features in both models is that the gas pressure is strongly peaked at the expanding shell front. Finally, ionizing momentum transfer roughly traces the neutral gas density and is therefore dynamically unimportant once the gas is ionized.

3.2 Velocity offset

We now consider whether the models self-consistently reproduce the velocity offset observed between the Lyα and He II lines. Figure 4 shows the typical Lyα line flux for the Pop III and MBH models from early to late times of 0.5 Myr, 3 Myr, and 8 Myr. Although each simulation environment is highly ionized by this time the two sources yield vastly different spectral profiles. This may be understood in terms of the residual H I within the expanding shell. As seen from Table 1, the Pop III source has a much higher hydrogen effective ionization cross-section than the black hole emission. In fact, the degree of ionization is such that Lyα photons emerge without a significant systemic velocity offset. On the other hand, the ionizing radiation in the MBH model leaves sufficient H I so that Lyα resonant scattering becomes coupled to the outflow. Therefore, the observed velocity offset provides a powerful hint into the nature of CR7 and provides an argument against a 10^5 K blackbody radiation source as might be produced from Pop III stars. In Figure 5 we show the time evolution of the velocity offset for the red peak of the intrinsic line-of-sight flux, which is fairly constant throughout the simulations demonstrating the robustness of these models.

We use the frequency dependent transmission curve of Laursen et al. (2011) to account for subsequent scattering of Lyα photons out of the line of sight. Specifically, we use their "benchmark" Model 1 curve at $z \approx 6.5$ as described in relation to their figures 2 and 3. The curve is a statistical average of a large number of sightlines ($\gtrsim 10^3$) cast from several hundreds of galaxies through a simulated cosmological volume. Any IGM model should be considered in the context of statistical variations depending on the particular galaxy and sightline. However, for concreteness we multiply their average IGM transmission curve with our intrinsic Lyα spectra when discussing the CR7 observables for the Laursen et al. (2011) model.

Our second treatment of transmission through the IGM represents a plausible reprocessing of the spectrum based on the analytic prescription of Madau & Rees (2000). Lyα photons are removed from the line of sight flux according to their likelihood of undergoing even a single scattering event. In an Einstein-de Sitter universe with a uniform, neutral IGM the optical depth of the red damping wing of the Gunn-Peterson (GP) trough is

$$\tau_{GP}^{red} = \frac{\tau_0(z)}{\pi R_\alpha^{-1}} \left(1 - \frac{\Delta v}{c}\right)^{3/2} \int_{x_{re}}^{x_{H\,II}} \frac{dx\, x^{9/2}}{(1-x)^2 + R_\alpha^2 x^6}\,, \quad (6)$$

where $R_\alpha \equiv \Lambda_\alpha \lambda_\alpha/(4\pi c) \approx 2\times10^{-8}$, the optical depth at line centre is $\tau_0(z) \approx 5\times10^5\,[(1+z)/7.7]^{3/2}$, and the dimensionless parameters are given by $x_i = (1-\Delta v/c)(1+z_i)/(1+z)$. The limits of integration are set by a cutoff at the reionization redshift $z_{re} \approx 6$ and the size of the ionized bubble around the source via $z_{H\,II}$ corresponding to a physical radius of $r_{H\,II} \approx 500$ kpc. Calculations of Lyα observables are based on the intrinsic line of sight flux attenuated by this approximate transmission through the IGM, i.e. $F_{\lambda,obs} \equiv F_\lambda e^{-\tau_{IGM}}$. As illustrated in Fig. 4 the observed luminosity may be reduced substantially with a ratio of $L/L_{obs} \approx 46$ and ≈ 1.6 for the Pop III and MBH cases, respectively, under the Laursen et al. (2011) IGM model. For the τ_{GP}^{red} IGM model the ratio is $L/L_{obs} \approx 7.7$ and ≈ 4.7 for the Pop III and MBH cases.

3.3 Spatial extent

An additional observational constraint from CR7 is the $\sim$ 16 kpc spatial extent of the Lyα emitting region. To examine this we show the evolution of the radial Lyα surface brightness profile in Fig. 6 for the Pop III and MBH models. As the shell expands the central intensity is reduced while the outer intensity increases. The drop in brightness at the shell front is much sharper in the black hole model than the Pop III case due to the more efficient Lyα trapping. The observed surface brightness reflects the estimated transmission through the IGM based on the models of Laursen et al. (2011) and that of Equation (6). Photons that scatter toward an observer at larger radii are typically closer to line centre and therefore suffer greater absorption. Specifically, for the MBH model we find an intrinsic to observed ratio of $SB_r/SB_{r,obs} \approx \{1.2, 2, 7, 20\}$ at $r \approx \{0.05, 1, 10, 20\}$ kpc, respectively, under the Laursen et al. (2011) IGM model. For the τ_{GP}^{red} IGM model the ratio is $SB_r/SB_{r,obs} \approx \{4, 6.5, 7.5\}$ at $r \approx \{0.05, 1, 20\}$ kpc, respectively.

Complementary to the radial surface brightness profile is the spectral line intensity as would be observed along a slit in the radial direction. Figure 7 illustrates such a measurement for the MBH model at simulation times of 3 Myr and 60 Myr. The images have been corrected for IGM transmission and show the relative importance of the red peak compared to the blue peak which is visible due to the logarithmic scaling. This perspective also demonstrates

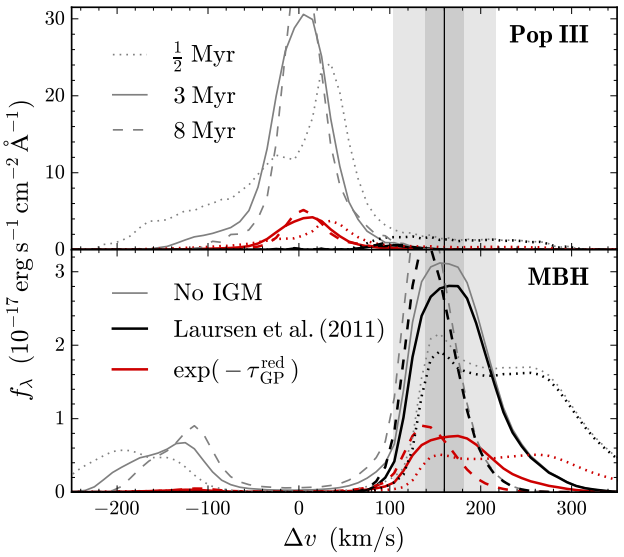


Figure 4. Observed line-of-sight flux as a function of Doppler velocity $\Delta v = c\Delta\lambda/\lambda$ for the Pop III and MBH models. The grey curves are intrinsic profiles while the black and red curves represent a plausible reprocessing due to scattering in the IGM based on the model from Laursen et al. (2011) and $\tau_{\rm GP}^{\rm red}$ from Equ. (6), respectively. These are shown for early to late times of 0.5 Myr (dotted), 3 Myr (solid), and 8 Myr (dashed). The observed velocity offset of +160 km s^{-1} (vertical line) is roughly reproduced in the MBH case but not in the Pop III model. The uncertainty due to DEIMOS/Keck and X-SHOOTER/VLT spectral resolution is illustrated by the grey vertical regions (see Section 2.1 for additional details).

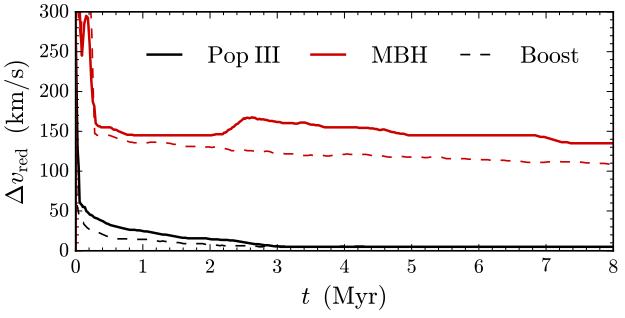


Figure 5. The time evolution of the velocity offset for the red peak of the intrinsic line-of-sight flux. The Pop III and MBH models are shown by the solid black and red curves, while the Boost modification is denoted by dashed curves of the corresponding color. The location of the offset is fairly constant throughout the simulations.

a slight decrease in the velocity offset at larger radii which is explained by the resonant scattering bias to return to line-centre. The primary difference between the early and late times is the radius of the shell front which by 60 Myr has advanced to $\sim$ 4 kpc and $\sim$ 8 kpc in the MBH and MBH Boost models, respectively. At later times the velocity offset decreases, possibly as a result of the lower shell velocity and a more diffuse Lyα trapping environment. Still, all of the aforementioned Lyα features persist in simulations carried out to 120 Myr. If the shell radius is indicative of the Lyα emitting region then even at $v_{\rm sh} \sim 100$ km s^{-1} it would take at least 50 Myr to achieve a size of $\sim$ 10 kpc in diameter. Although our models allow $v_{\rm sh}$ to be a few times larger, we nonetheless find it less probable that the CR7 source is significantly younger than this. Again, such long source durations can more easily be explained within a MBH scenario than a Pop III starburst.

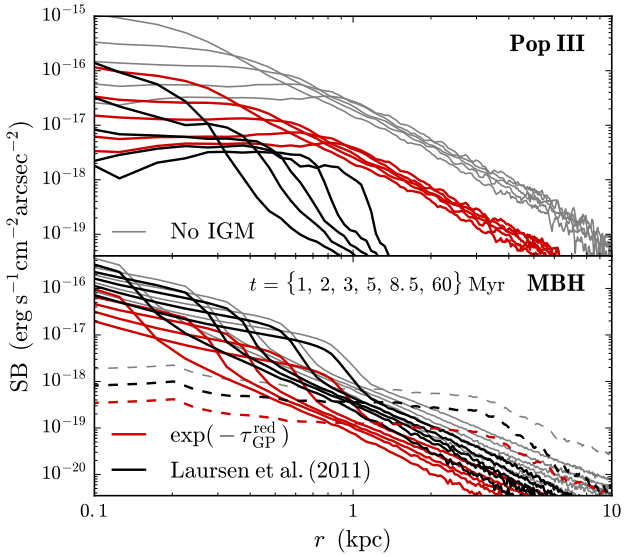


Figure 6. Evolution of the radial surface brightness profile for the Pop III and MBH models at $t = \{1, 2, 3, 5, 8.5, 60\}$ Myr. The late dashed curve is from a simulation with lower spatial resolution. For the intrinsic grey curves the region is more uniform and extended in the Pop III case while the MBH emission more closely follows the shell expansion as a result of increased Lyα trapping. The black and red curves are corrected for transmission through the IGM based on the model from Laursen et al. (2011) and $\tau_{\rm GP}^{\rm red}$ from Equ. (6), respectively. After scattering in the IGM the Pop III model appears much more compact whereas the MBH model remains spatially extended.

3.4 Caveats

We now discuss the limitations of our simulations and their potential impact on the above results. Uncertainties in the galaxy model parameters and initial conditions may produce slightly different observables. For example, normalizing the black hole flux to the observed He II emission leads to a much lower Lyα luminosity. For this reason we have explored the "Boost" and "Leak" models to determine the impact of extra Lyα emission or less ionizing radiation. We also modeled the photon emission as a central point source. While the Pop III starburst is initially centrally dominated, it is highly unlikely to remain so as star formation proceeds. However, similar to Dijkstra & Loeb (2008) we expect our final results are not particularly sensitive to the choice for the radial Lyα photon emission.

Another issue is that of numerical resolution. At a halo mass of $M_{\rm vir} \approx 3 \times 10^{10}$ M$_\odot$ we achieve Lagrangian mass elements of $\approx 6.6 \times 10^5$ M$_\odot$ which at various times corresponds to $\approx 0.1 - 2$ pc resolution at the shell front. Improving the resolution by a factor of ≈ 5 produces very similar results except at the earliest times or innermost radii. Higher resolution leads to slightly faster initial velocities because higher densities allow for more efficient radiation coupling. However, the computational cost may change dramatically based on the number of timesteps with MCRT calculations and the convergence criteria. To be safe we require that between

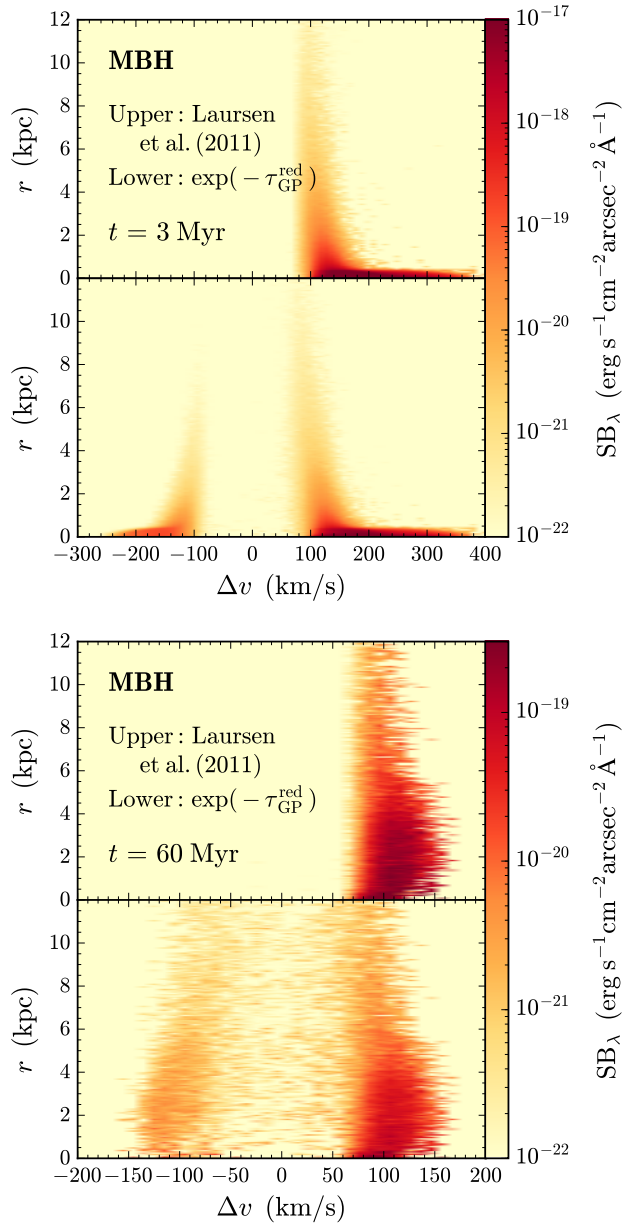


Figure 7. The spectral line intensity as a function of radius for the MBH model at early (t = 3 Myr) and late (t = 60 Myr) times. In the ensuing time the shell radius has expanded from $r_{\rm sh} \approx 0.5$ kpc to $r_{\rm sh} \approx 4$ kpc, which makes a visible difference in the extent of the Lyα emitting region. The images are corrected for transmission through the IGM where the upper and lower panels are based on the model from Laursen et al. (2011) and $\tau^{\rm red}_{\rm GP}$ from Equ. (6), respectively.

batches of ≈ 1600 photons the Lyα force has a $\lesssim 1$ per cent relative change in $\gtrsim 99$ per cent of the cells.

Furthermore, distinguishing effects due to radiative transfer within the galaxy and in the IGM can be difficult to disentangle. We have used two IGM transmission models based on cosmological simulations and a simple analytic treatment. Still, the true Lyα transmission could deviate from each of these. See Dijkstra (2014) for a review containing a detailed discussion and related references. An important consequence of some IGM models is that the observed velocity offset could be mimicked by a broad spectrum or a static double-peaked spectrum in which the flux blueward of the observed +160 km s^{-1} offset is suppressed by inflow into the potential well (Loeb & Eisenstein 1995; Barkana & Loeb 2003). Future observations could potentially distinguish between these scenarios.

We also note that the input spectrum impacts other Lyα observables. For example, in Fig. 4 the emergent spectra have FWHM at 0.5 Myr, 3 Myr, and 8 Myr of respectively $\approx$ 60 km s^{-1}, 70 km s^{-1}, and 50 km s^{-1} for the Pop III model and $\approx$ 180 km s^{-1}, 100 km s^{-1}, and 60 km s^{-1} for the MBH model. All of these values are significantly narrower than the observed 266 ±15 km s^{-1} FWHM of the Lyα line. This indicates that the width is dominated by unresolved turbulence and three-dimensional radiative transfer effects. As a rough estimate we assume FWHM $\propto v_{\rm eff} \approx (c_{\rm s}^2 + v_{\rm turb}^2)^{1/2} \approx c_{\rm s}(1+{\rm Ma}^2)^{1/2} \approx c_{\rm s}{\rm Ma}$, where Ma is the Mach number. A comparison with the calculated FWHM implies Ma $\approx 2-5$, which is reasonable but not incorporated into our simulations. We may also compare our results with the observed line ratio of He II/Ly$\alpha \approx 0.22$. At 3 Myr with the Laursen et al. (2011) ($\tau^{\rm red}_{\rm GP}$) IGM transmission we find He II/Ly$\alpha \approx 3.36$ (0.37) for the Pop III model and He II/Ly$\alpha \approx 0.41$ (1.4) for the MBH model. All of these are high by a factor of $\gtrsim 2$, which is difficult to account for in the Pop III case but the MBH case may allow for more Lyα photons than inferred by the Compton-thick spectrum. The 'boost' modification explores the effect of an order of magnitude overcorrection to this ratio. Finally, this ratio is also sensitive to the statistical uncertainty in IGM modeling. We also note that several effects might diminish Lyα radiation in high-density environments (Neufeld 1990). Recently, Dijkstra et al. (2016) argued that collisional de-excitation plays an important role for Lyα signatures of DCBHs. Our simulations do not resolve such high densities but these effects could be incorporated into the input spectrum, e.g. with a broader Lyα line. Although the He II/Lyα line ratio is affected, we do not expect significant changes to the Lyα spectral profile or surface brightness profile.

Perhaps the most important caveat is that although we accurately incorporate Lyα trapping, ionizing radiation, chemistry, and cooling into our hydrodynamical study we have done so in spherical symmetry. The one-dimensional approximation provides significant insight into the CR7 source. However, three-dimensional effects are likely to be important. For example, geometric effects such as gas clumping, rotation, filamentary structure, and anisotropic emission from the source often lead to anisotropic escape, photon leakage, or otherwise altered dynamical impact. This may increase the amount of residual H I within the galaxy and perhaps more naturally reproduce the observed velocity offset. One might consider adding a layer of complexity with semi-analytic prescriptions within our one-dimensional models, e.g. self-shielding clouds or low column density holes. However such alterations would no longer be hydrodynamically self-consistent. Although three-dimensional hydrodynamical simulations exist they do not incorporate fully-coupled Lyα feedback. Post-processing studies of Lyα radiative transfer in similar contexts provides insight about the impact of three-dimensional effects (Dijkstra & Kramer 2012; Behrens et al. 2014; Duval et al. 2014; Zheng & Wallace 2014; Smith et al. 2015). Lyα observables are certainly affected by viewing angle with higher equivalent widths, escape fractions, and line-of-sight fluxes for face-on inclinations than edge-on directions, e.g. due to the formation of a disk or jet. Three-dimensional simulations also demonstrate the importance of small-scale structure in the interstellar medium. Both of these effects could change the He II/Lyα line ratio by a factor of a few. Additional uncertainties in the galaxy model parameters and initial conditions may produce different ob-

servables. For example, Lyα feedback and radiative transfer observables may be affected by altering the gas density profile. Our choice of an isothermal profile is an idealized setup that may affect the early gas dynamics but matters less as the system evolves, especially in relation to the expanding shell. Our model uncertainties are likely dominated by our overall assumption of a one-dimensional geometry as opposed to the details of this one-dimensional profile. Still, in the context of the CR7 galaxy the assumption of spherical symmetry ought to provide a qualitatively correct, first-order, prediction of the Lyα signature.

4 SUMMARY AND CONCLUSIONS

Lyα emitting sources provide intriguing hints about the formation and evolution of galaxies in the high-redshift universe. The CR7 source at $z \approx 6.6$ presents a unique opportunity in this regard due to its exceptionally bright Lyα and He II 1640 Å line emission but absence of metal lines. Previous investigations have considered the possibility that we are witnessing a young primordial starburst or direct collapse black hole. In this work we examine the connection between the emission source and Lyα observables. Specifically, Sobral et al. (2015) report a $+160$ km s^{-1} velocity offset between the Lyα and He II line peaks which we self-consistently reproduce in one-dimensional radiation-hydrodynamics simulations. Our simulations represent the first hydrodynamical study incorporating accurate Monte-Carlo radiative transfer calculations of Lyα radiation pressure. The CR7 galaxy is an ideal application as it allows direct comparison with current observations.

In this pristine environment the dominant physical processes are gravity, hydrodynamical gas pressure, and radiative feedback from Lyα photons as well as the thermal and chemical coupling of ionizing radiation. The source ionizes its own local bubble and drives an expanding shell of gas from the centre. The details depend on the properties of the source spectrum which we categorize as either a Pop III star cluster with 10^5 K blackbody emission or a massive black hole with a nonthermal Compton-thick spectrum. Our results may be summarized as follows:

(1) The MBH model results in greater photon trapping within the shell because the harder spectrum reduces the average ionization cross-section for hydrogen yielding extra residual H I.
(2) The extent of the Lyα emitting region is correlated with the shell radius implying a likely source lifetime of $10 - 100$ Myr.
(3) The MBH model reproduces the $+160$ km s^{-1} velocity offset and the 16 kpc region size while the Pop III model does not.

We emphasize that these models represent a particular choice for the spectral energy distribution and should be viewed as such. Nonetheless, our results provide evidence corroborating a direct collapse black hole scenario. Indeed, we have presented independent and complementary evidence that CR7 hosts a DCBH, next to arguments based on metal enrichment which assesses the likelihood of forming Pop III stars around $z \approx 6.6$ in massive host systems (e.g. Hartwig et al. 2015). It is known that a strong background of Lyman-Werner radiation is able to suppress star formation until the buildup of atomic cooling haloes, i.e. systems with virial temperature $T_{\rm vir} \gtrsim 10^4$ K such that Lyα cooling is enabled (e.g. Haiman et al. 1997). Furthermore, Visbal et al. (2016) demonstrate that if local reionization occurs early enough and with sufficient ionizing flux the photoheated gas around a $M_{\rm vir} \sim 10^9$ M$_\odot$ halo with star-free progenitors has a cosmological Jeans mass that is comparably large. In such cases the metal enrichment is considerably delayed and potentially results in a rapid Pop III starburst with Lyα luminosity comparable to that of CR7. However, the Lyα signatures are still more easily explained by the DCBH scenario.

Finally, we briefly discuss additional observational signatures that may distinguish a DCBH from a Pop III starburst. The formation of a DCBH is likely to generate rapid rotation, producing a jet. However, CR7 was not detected in the Chandra COSMOS Survey so its X-ray luminosity in the energy range $0.2 - 10$ keV is below 10^{44} erg s^{-1} (Elvis et al. 2009). This is not surprising because such a large flux would indicate the jet is pointing directly towards us. At other angles the low disk temperature, high-z suppression factor, and absorption in the Milky Way imply an even lower observed flux (Hartwig et al. 2015), pushing the limits of even next-generation X-ray observatories, such as the X-ray Surveyor (Weisskopf et al. 2015). On the other hand, a detection of radio emission would also provide strong evidence for the presence of a massive black hole. Future improved simulations are likely to further elucidate the nature of the remarkable CR7 source, allowing more robust predictions for its multi-wavelength signature.

ACKNOWLEDGEMENTS

We thank the referee for constructive comments and suggestions which have improved the quality of this work. AS thanks the Institute for Theory and Computation (ITC) at the Harvard-Smithsonian Center for Astrophysics for hosting him as a visitor through the National Science Foundation Graduate Research Internship Program. This material is based upon work supported by a National Science Foundation Graduate Research Fellowship. VB acknowledges support from NSF grant AST-1413501, and AL from NSF grant AST-1312034. The authors acknowledge the Texas Advanced Computing Center (TACC) at the University of Texas at Austin for providing HPC resources.

REFERENCES

Abel T., Norman M. L., Madau P., 1999, ApJ, 523, 66
Agarwal B., Johnson J. L., Zackrisson E., Labbe I., van den Bosch F. C., Natarajan P., Khochfar S., 2015, MNRAS, preprint (arXiv:1510.01733)
Barkana R., Loeb A., 2003, Nature, 421, 341
Behrens C., Dijkstra M., Niemeyer J. C., 2014, A&A, 563, A77
Bouwens R. J., et al., 2011, ApJ, 737, 90
Brinchmann J., Pettini M., Charlot S., 2008, MNRAS, 385, 769
Bromm V., Loeb A., 2003, ApJ, 596, 34
Bromm V., Yoshida N., 2011, ARA&A, 49, 373
Bromm V., Kudritzki R. P., Loeb A., 2001, ApJ, 552, 464
Bromm V., Coppi P. S., Larson R. B., 2002, ApJ, 564, 23
Castor J. I., 2004, Radiation Hydrodynamics. Cambridge Univ. Press, Cambridge, UK
Cen R., 1992, ApJS, 78, 341
Dijkstra M., 2014, Publ. Astron. Soc. Australia, 31, e040
Dijkstra M., Kramer R., 2012, MNRAS, 424, 1672
Dijkstra M., Loeb A., 2008, MNRAS, 391, 457
Dijkstra M., Loeb A., 2009, MNRAS, 396, 377
Dijkstra M., Gronke M., Sobral D., 2016, ApJ, preprint (arXiv:1602.07695)
Duval F., Schaerer D., Östlin G., Laursen P., 2014, A&A, 562, A52
Elvis M., et al., 2009, ApJS, 184, 158
Erb D. K., et al., 2014, ApJ, 795, 33
Fan X., et al., 2006, AJ, 131, 1203
Finkelstein S. L., et al., 2013, Nature, 502, 524
Geach J. E., et al., 2014, Nature, 516, 68
Haiman Z., Rees M. J., Loeb A., 1997, ApJ, 476, 458
Hartwig T., et al., 2015, MNRAS, preprint (arXiv:1512.01111)

Hashimoto T., et al., 2015, ApJ, 812, 157
Jensen H., Laursen P., Mellema G., Iliev I. T., Sommer-Larsen J., Shapiro P. R., 2013, MNRAS, 428, 1366
Jeon M., Pawlik A. H., Bromm V., Milosavljević M., 2014, MNRAS, 440, 3778
Jeon M., Bromm V., Pawlik A. H., Milosavljević M., 2015, MNRAS, 452, 1152
Johnson J. L., Greif T. H., Bromm V., Klessen R. S., Ippolito J., 2009, MNRAS, 399, 37
Kakiichi K., Dijkstra M., Ciardi B., Graziani L., 2015, MNRAS, preprint (arXiv:1510.05647)
Laursen P., Sommer-Larsen J., Razoumov A. O., 2011, ApJ, 728, 52
Loeb A., Eisenstein D. J., 1995, ApJ, 448, 17
Loeb A., Furlanetto S. R., 2013, The First Galaxies in the Universe. Princeton Univ. Press, Princeton, NJ
Loeb A., Rybicki G. B., 1999, ApJ, 524, 527
Ma Q., Maio U., Ciardi B., Salvaterra R., 2015, MNRAS, 449, 3006
Madau P., Rees M. J., 2000, ApJ, 542, L69
Matthee J., Sobral D., Santos S., Röttgering H., Darvish B., Mobasher B., 2015, MNRAS, 451, 400
Mesinger A., Aykutalp A., Vanzella E., Pentericci L., Ferrara A., Dijkstra M., 2015, MNRAS, 446, 566
Mezzacappa A., Bruenn S. W., 1993, ApJ, 405, 669
Neufeld D. A., 1990, ApJ, 350, 216
Oesch P. A., et al., 2015, ApJ, 804, L30
Pacucci F., Ferrara A., Volonteri M., Dubus G., 2015, MNRAS, 454, 3771
Pallottini A., Ferrara A., Gallerani S., Salvadori S., D'Odorico V., 2014, MNRAS, 440, 2498
Pallottini A., et al., 2015, MNRAS, 453, 2465
Partridge R. B., Peebles P. J. E., 1967, ApJ, 147, 868
Pawlik A. H., Schaye J., 2011, MNRAS, 412, 1943
Pawlik A. H., Milosavljević M., Bromm V., 2011, ApJ, 731, 54
Pawlik A. H., Milosavljević M., Bromm V., 2013, ApJ, 767, 59
Schaerer D., 2002, A&A, 382, 28
Shull J. M., van Steenberg M. E., 1985, ApJ, 298, 268
Smidt J., Wiggins B. K., Johnson J. L., 2016, ApJ, preprint (arXiv:1603.00888)
Smith A., Safranek-Shrader C., Bromm V., Milosavljević M., 2015, MNRAS, 449, 4336
Smith A., Bromm V., Loeb A., 2016, MNRAS, to be submitted
Sobral D., Matthee J., Darvish B., Schaerer D., Mobasher B., Röttgering H. J. A., Santos S., Hemmati S., 2015, ApJ, 808, 139
Stark D. P., et al., 2015, MNRAS, 450, 1846
Steidel C. C., Erb D. K., Shapley A. E., Pettini M., Reddy N., Bogosavljević M., Rudie G. C., Rakic O., 2010, ApJ, 717, 289
Visbal E., Haiman Z., Bryan G. L., 2016, MNRAS, preprint (arXiv:1602.04843)
Weisskopf M. C., Gaskin J., Tananbaum H., Vikhlinin A., 2015. eprint: arXiv:1505.00814, http://adsabs.harvard.edu/abs/2015SPIE.9510E..02W
Yang H., Malhotra S., Gronke M., Rhoads J. E., Dijkstra M., Jaskot A., Zheng Z., Wang J., 2016, ApJ, 820, 130
Zheng Z., Wallace J., 2014, ApJ, 794, 116
Zitrin A., et al., 2015, ApJ, 810, L12
von Neumann J., Richtmyer R. D., 1950, J. Appl. Phys., 21, 232

This paper has been typeset from a TEX/LATEX file prepared by the author.